



HAL
open science

Mass Calibration of the CODEX Cluster Sample using SPIDERS Spectroscopy - I. The Richness-Mass Relation

R. Capasso, J.J. Mohr, A. Saro, A. Biviano, N. Clerc, A. Finoguenov, S. Grandis, C. Collins, G. Erfanianfar, S. Damsted, et al.

► To cite this version:

R. Capasso, J.J. Mohr, A. Saro, A. Biviano, N. Clerc, et al.. Mass Calibration of the CODEX Cluster Sample using SPIDERS Spectroscopy - I. The Richness-Mass Relation. Monthly Notices of the Royal Astronomical Society, 2019, 486 (2), pp.1594-1607. 10.1093/mnras/stz931 . hal-01974842

HAL Id: hal-01974842


<https://hal.science/hal-01974842>

Submitted on 5 Jul 2023

HAL is a multi-disciplinary open access archive for the deposit and dissemination of scientific research documents, whether they are published or not. The documents may come from teaching and research institutions in France or abroad, or from public or private research centers.

L'archive ouverte pluridisciplinaire **HAL**, est destinée au dépôt et à la diffusion de documents scientifiques de niveau recherche, publiés ou non, émanant des établissements d'enseignement et de recherche français ou étrangers, des laboratoires publics ou privés.

Mass calibration of the CODEX cluster sample using SPIDERS spectroscopy – I. The richness–mass relation

R. Capasso ^{1,2★} J. J. Mohr,^{1,2,3} A. Saro,^{1,2,4} A. Biviano,⁴ N. Clerc,^{3,5}
A. Finoguenov,^{3,6} S. Grandis,^{1,2} C. Collins,⁷ G. Erfanianfar,³ S. Damsted,⁶
C. Kirkpatrick⁶ and A. Kukkola⁶

¹Faculty of Physics, Ludwig-Maximilians-Universität, Scheinerstr. 1, D-81679 Munich, Germany

²Excellence Cluster Universe, Boltzmannstr. 2, D-85748 Garching, Germany

³Max Planck Institute for Extraterrestrial Physics, Giessenbachstr., D-85748 Garching, Germany

⁴INAF – Osservatorio Astronomico di Trieste via G.B. Tiepolo 11, I-34143 Trieste, Italy

⁵IRAP, Université de Toulouse, CNRS, UPS, CNES, Toulouse, France

⁶Department of Physics, University of Helsinki, Gustaf Hällströmin katu 2a, FI-00014 Helsinki, Finland

⁷Astrophysics Research Institute, Liverpool John Moores University, IC2, Liverpool Science Park, 146 Brownlow Hill, Liverpool L3 5RF, UK

Accepted 2019 March 29. Received 2019 March 27; in original form 2018 December 14

ABSTRACT

We use galaxy dynamical information to calibrate the richness–mass scaling relation of a sample of 428 galaxy clusters that are members of the CODEX sample with redshifts up to $z \sim 0.7$. These clusters were X-ray selected using the ROSAT All-Sky Survey (RASS) and then cross-matched to associated systems in the redMaPPer (the red sequence Matched-filter Probabilistic Percolation) catalogue from the Sloan Digital Sky Survey. The spectroscopic sample we analyse was obtained in the SPIDERS program and contains ~ 7800 red member galaxies. Adopting NFW mass and galaxy density profiles and a broad range of orbital anisotropy profiles, we use the Jeans equation to calculate halo masses. Modelling the scaling relation as $\lambda \propto A_\lambda M_{200c}^{B_\lambda} (1+z)^{\gamma_\lambda}$, we find the parameter constraints $A_\lambda = 38.6_{-4.1}^{+3.1} \pm 3.9$, $B_\lambda = 0.99_{-0.07}^{+0.06} \pm 0.04$, and $\gamma_\lambda = -1.13_{-0.34}^{+0.32} \pm 0.49$, where we present systematic uncertainties as a second component. We find good agreement with previously published mass trends with the exception of those from stacked weak lensing analyses. We note that although the lensing analyses failed to account for the Eddington bias, this is not enough to explain the differences. We suggest that differences in the levels of contamination between pure redMaPPer and RASS + redMaPPer samples could well contribute to these differences. The redshift trend we measure is more negative than but statistically consistent with previous results. We suggest that our measured redshift trend reflects a change in the cluster galaxy red sequence (RS) fraction with redshift, noting that the trend we measure is consistent with but somewhat stronger than an independently measured redshift trend in the RS fraction. We also examine the impact of a plausible model of correlated scatter in X-ray luminosity and optical richness, showing it has negligible impact on our results.

Key words: galaxies: clusters: general – galaxies: evolution – galaxies: kinematics and dynamics – large-scale structure of Universe.

1 INTRODUCTION

The formation and evolution of galaxy clusters is governed by the complex interplay between the gravity-induced dynamics of collapse and the baryonic processes associated with galaxy formation. Galaxy clusters, thus, constitute unique laboratories for both astrophysics and cosmology. On one side, the abundance of these

objects as a function of mass and redshift is a well-established cosmological probe (e.g. White, Efstathiou & Frenk 1993; Haiman, Mohr & Holder 2001; Mantz et al. 2015; de Haan et al. 2016). On the other side, the observation of the evolution of galaxy properties in clusters provide us with information on galaxy formation, their assembly history, and the correlation between their evolution and environment (e.g. Dressler 1984; de Propris et al. 1999; Mei et al. 2009; Muzzin et al. 2012; Hennig et al. 2017; Strazzullo et al. 2018; Capasso et al. 2019).

* E-mail: Raffaella.Capasso@physik.uni-muenchen.de

Of primary importance to both types of studies are accurate mass estimates and large samples of clusters with well-understood selection. For cosmological studies that adopt the halo mass function this is obvious, but for galaxy population studies it is equally important, because galaxy properties vary with clustercentric distance, and thus to compare properties of clusters across a range of mass and redshift, it is crucial to be able to adopt a meaningful overdensity radius such as r_{200c} , which corresponds to the radius at which the mean enclosed density is 200 times the critical density and is thus trivially derived from the corresponding mass M_{200c} . Adopting an overdensity radius reveals cluster regularity or approximate self-similarity in structure formation simulations (e.g. Navarro, Frenk & White 1997) and has also revealed regularity in studies of real clusters (e.g. Pratt et al. 2007).

A good understanding of the mass–observable relation that links the mass of galaxy clusters to readily obtainable observables such as the optical richness λ is then more than a convenience. It enables both cosmological and structure formation studies on large cluster ensembles. Within this context, uncertainties on cluster masses include the measurement uncertainties on the observable, the intrinsic scatter in the observable at fixed mass and redshift and the uncertainties on the parameters of the mass–observable relation. The latter can be controlled through calibration.

Different mass constraints have been used to calibrate the mass–observable relation for cluster ensembles, each with its advantages and disadvantages. Weak lensing distortions of background galaxies by clusters can be used to provide accurate cluster mass estimates (e.g. Corless & King 2009; Becker & Kravtsov 2011; Dietrich et al. 2018; McClintock et al. 2018). However, mass measurements from weak gravitational lensing of background galaxies become extremely challenging at high redshift $z \sim 1$, where the number of background sources in typical imaging datasets drops, weakening the mass constraints. Moreover, the scatter between weak lensing inferred masses and true halo mass is large, implying that large numbers of clusters are needed for accurate mass calibration. Recently, Baxter et al. (2018) applied gravitational lensing of the cosmic microwave background (CMB), using CMB maps from the South Pole Telescope (SPT) 2500 deg² SPT–SZ survey, demonstrating an ability to constrain the amplitude of the λ –mass relation to ~ 20 per cent accuracy. This offers great promise for the future, assuming systematic biases due to the thermal Sunyaev–Zel’dovich effect (SZE) and cluster miscentring can be accurately corrected. Cluster velocity dispersions, obtained through spectroscopic observations of cluster member galaxies, have proven to be good mass proxies as well, due in part to their insensitivity to complex intra-cluster medium (ICM) physics. But as with weak lensing masses, dispersion-based masses still show large percluster scatter (Evrard et al. 2008; Saro et al. 2013; Sifón et al. 2013; Ruel et al. 2014), implying that large samples must be used for mass calibration.

In this work, we aim to calibrate the λ –mass–redshift scaling relation parameters by performing a dynamical analysis based on the Jeans equation (Binney & Tremaine 1987). In particular, we use a modification of the MAMPOSSt technique (Modeling Anisotropy and Mass Profiles of Observed Spherical Systems; Mamon, Biviano & Boué 2013), which fits the distribution of particles in the observed projected phase space [line-of-sight (LOS) velocities and distribution as a function of projected radius], to use the full information in the LOS velocity distribution and projected positions of cluster galaxies. This method has been extensively used to recover dynamical masses and gain information on galaxy formation and evolution (e.g. Biviano et al. 2013, 2017; Munari, Biviano & Mamon 2014). In particular, in Capasso et al. (2019), it was demonstrated

that, using this method on a composite cluster with ~ 600 cluster members, dynamical masses, and orbital anisotropy of the galaxy population can be simultaneously constrained, delivering masses with a ~ 15 per cent uncertainty (decreasing to ~ 8 per cent when using a composite cluster with ~ 3000 tracers). In addition, it was shown that combining cluster dynamical constraints in likelihood space produces final mass constraints that are consistent with masses from composite or stacked cluster analyses.

We perform a dynamical analysis on the ROSAT All-Sky Survey (RASS) X-ray cluster candidates, which have optical counterparts in Sloan Digital Sky Survey (SDSS) imaging data identified using the redMaPPer algorithm (the red sequence Matched-filter Probabilistic Percolation algorithm, Rykoff et al. 2014, see Section 2.1). The resulting cluster catalogue is called CODEX (CONstrain Dark Energy with X-ray clusters; Finoguenov et al. in preparation), and a subset of these clusters have since been spectroscopically studied within the SPectroscopic IDentification of eRosita Sources (SPIDERS) survey (Clerc et al. 2016). The analysis carried out here includes a sample of 428 CODEX clusters with a corresponding sample of ~ 7800 red member galaxies with measured redshifts. The clusters span the redshift range $0.03 \leq z_c \leq 0.66$, with richness $20 \leq \lambda \leq 230$.

The paper is organized as follows: in Section 2, we summarize the data set used for our analysis. In Section 3, we give an overview of the theoretical framework. The results are presented in Section 4, where we discuss the outcome of our mass–observable relation calibration, and we present our conclusions in Section 5. Throughout this paper, we adopt a flat Λ cold dark matter (Λ CDM) cosmology with a Hubble constant $H_0 = 70 \text{ km s}^{-1} \text{ Mpc}^{-1}$, and a matter density parameter $\Omega_M = 0.3$. Cluster masses (M_{200c}) are defined within r_{200c} , the radius within which the cluster overdensity is 200 times the critical density of the Universe at the cluster redshift. We refer to r_{200c} simply as the virial radius. All quoted uncertainties are equivalent to Gaussian 1σ confidence regions unless otherwise stated.

2 DATA

This work is based on a spectroscopic galaxy sample constructed within the SPIDERS survey (Clerc et al. 2016), which observed a subset of CODEX galaxy clusters. These clusters were selected from the RASS (see Voges et al. 1999) and then cross-matched with nearby optically selected systems identified using the redMaPPer algorithm applied to the SDSS-IV (see Dawson et al. 2016; Blanton et al. 2017) optical imaging data. In the following section, we describe each of these elements of the dataset.

2.1 The redMaPPer algorithm

redMaPPer is an optical cluster-finding algorithm based on the red sequence (RS) technique, built around the richness estimator of Rykoff et al. (2012). It has been successfully applied to photometric data from the Eighth Data Release (DR8; Aihara et al. 2011) of the SDSS, and subsequently to the SDSS Stripe 82 co-add data (Annis et al. 2014) and to the Dark Energy Survey (DES) Science Verification Data (SV) and Year 1 (Y1) data (Saro et al. 2015; Rykoff et al. 2016; Soergel et al. 2016). It has been shown to provide excellent photometric redshift performance and optical richness estimates λ that tightly correlate with external mass proxies.

The optical catalogue construction is performed in several steps. First of all, the RS model is calibrated on a set of clusters having spectroscopic redshifts. This model is then used to identify galaxy clusters and measure their richness. To each galaxy in the vicinity of a galaxy cluster, redMaPPer estimates the membership probability,

$P_{\text{mem}} \in [0, 1]$, based on its magnitude, colours, and clustercentric distance. This probability is also used to estimate the richness of the cluster. The latter is thus defined as the sum of the membership probabilities (P_{mem}) over all galaxies $\lambda = \sum P_{\text{mem}}$.

2.2 The CODEX sample

The CODEX survey is designed to combine *ROSAT* X-ray cluster candidates with optical selected cluster candidates identified using redMaPPer algorithm (Rykoff et al. 2014, see Section 2.1). This catalogue is constructed in several steps. As a first step, RASS data are used to identify all X-ray sources with detection significance $S/N > 4$. The redMaPPer algorithm is then run on the SDSS imaging data around each RASS source position to identify candidate clusters with an RS, which constitutes a collection of passive galaxies lying at a common redshift. The redMaPPer algorithm provides an estimate for the photometric redshift of the cluster, an estimation of the optical richness and an optical cluster centre, which is constrained to be within 3 arcmin of the X-ray position. In cases of multiple optical counterparts meeting these criteria, the counterpart having the highest richness is assigned to the RASS X-ray source.

Using the updated optical position of the cluster, a revised RS is identified, providing the final estimate of the cluster photometric redshift and richness (optical or ‘OPT’ quantities: $z_{\lambda, \text{OPT}}$, λ_{OPT} , etc.). If the cluster is at sufficiently high redshift that the SDSS photometric data are not deep enough to allow a direct measurement of richness over a fixed fraction of the cluster galaxy luminosity function (i.e. to a limit $m_*(z) + \Delta$, where Δ is the same for all clusters), then a correction factor η is calculated and applied to the richness. As described in Section 4.1, this has an impact on the Poisson noise contribution to the richness and must be included in the analysis of the mass–observable scaling relation.

In the final step, X-ray properties based on the RASS count-rate and the redMaPPer redshift are calculated in optimized apertures (imposing a minimal signal-to-noise threshold of 1.6), assuming a model for the X-ray spectral emissivity, along with the aperture-corrected cluster flux f_X and [0.1–2.4] keV luminosities L_X . The final CODEX sample then results in X-ray-detected clusters, for which we have an estimate of the redshift, optical richness, the optical cluster centre, and X-ray luminosity. This sample has been used for follow-up observations of the SPIDERS survey, described below, which finally provided spectroscopic redshift estimates of cluster member galaxies.

2.3 The SPIDERS spectroscopic sample

The SPIDERS survey is an observational program aiming to obtain homogeneous and complete spectroscopic follow-up of extragalactic sources, using data from X-ray satellites that lie within the SDSS-IV imaging footprint. The driving goals of the program are the confirmation of X-ray-extended sources identified as galaxy cluster candidates and the assignment of a precise redshift. In the final years of SDSS-IV, SPIDERS will follow-up X-ray-extended sources extracted from the all sky X-ray eROSITA survey (extended ROentgen Survey with an Imaging Telescope Array, Predehl et al. 2010; Merloni et al. 2012). Prior to the launch of eROSITA, galaxy clusters identified in the shallower RASS and sparser *XMM-Newton* data will constitute the bulk of the SPIDERS program. The spectroscopy is obtained using the Baryon Oscillation Spectroscopic Survey (BOSS) spectrograph mounted on the SDSS-2.5m telescope at Apache Point Observatory (Gunn et al. 2006),

performing follow-up of galaxies detected in the large area of extragalactic sky imaged in *ugriz* filters by the same telescope. In the following sections, we describe the target selection, the cuts made on the sample, and how the spectroscopic galaxy sample used in this work is obtained.

2.3.1 Target selection

The target selection and initial cuts to the sample are outlined in Clerc et al. (2016). Here, we summarize the most salient features. To optimize the number of spectroscopically confirmed clusters, the redMaPPer membership probability P_{mem} is used as a reference to assign priorities to potential targets, ranking galaxies within each cluster. The algorithm starts with the richest cluster in the sample, iteratively proceeding to lower richness. The pool of targets along with the priority flag is then submitted to the eBOSS tiling algorithm. The final data reduction and spectral classification rely on the eBOSS spectroscopic pipeline and processing.

An automatic procedure is used to assign the membership of RS galaxies with measured redshifts. For each cluster, an iterative clipping procedure is performed. As a first step, members with velocity offsets greater than 5000 km s^{-1} (relative to this first guess mean redshift) are rejected. The remaining potential members $N_{z\text{-spec}}$ are used to estimate the velocity dispersion of the cluster, either using the biweight variance ($N_{z\text{-spec}} \geq 15$; see Beers, Flynn & Gebhardt 1990) or the gapper estimator (if $N_{z\text{-spec}} < 15$). Finally, a 3σ clipping is applied, rejecting objects lying further away than three times the velocity dispersion from the mean velocity.

A final validation of all galaxy clusters and assessment of their redshifts is achieved through visual screening of the outcome of the automatic procedure. Sometimes the automated procedure fails. This occurs, for example, if fewer than three members are assigned to a cluster, or if the initial 5000 km s^{-1} clipping rejected all members. The latter can occur when there are several distinct structures along the LOS. Independent inspectors analyse these complex cases, which may lead to inclusion or removal of members. This process sets the validation status and mean redshift of the cluster. LOS projection effects not disentangled by the photometric membership algorithm can also be identified and split into several components. Final cluster redshift estimates are based on the biweight average (Beers et al. 1990) of all RS galaxies selected as cluster members, if at least three members are assigned to the cluster. The typical cluster redshift statistical uncertainty is $\Delta_z/(1+z) \lesssim 10^{-3}$.

The updated cluster spectroscopic redshifts are then used to update the computation of X-ray cluster properties. Assuming the standard flat Λ CDM cosmological model (Hubble constant $H_0 = 70 \text{ km s}^{-1} \text{ Mpc}^{-1}$, and matter density parameter $\Omega_M = 0.3$, *ROSAT* fluxes are converted into rest-frame [0.1–2.4] keV luminosities and scaling relations allow an estimate of the cluster mass and characteristic radius r_{500} or r_{200c} . The typical measurement uncertainty on the luminosities of CODEX clusters amounts to ≈ 35 per cent, as computed from the Poissonian fluctuation in the associated *ROSAT* X-ray photons (see Mirkazemi et al. 2015).

2.3.2 Final spectroscopic cluster member sample

Given the sample produced as described above, we apply some additional cuts prior to our analysis. As mentioned above, there are cases in which a CODEX cluster has multiple groups of galaxies separated by a large velocity gap along the LOS. To avoid merging systems, we only use clusters which are flagged as having

one component along the LOS. We restrict our analysis to the cluster virial region ($R \leq r_{200c}$). Moreover, we exclude the very central cluster region ($R \leq 50$ kpc), to account for the positional uncertainties of cluster centres, and to avoid including the centrally located Brightest Cluster Galaxy (BCG) in the dynamical analysis. At the end of this process, our spectroscopic data set from SPIDERS consists of 705 galaxy clusters, for a total of $\approx 11\,400$ candidate cluster members, with a median redshift $z = 0.21$ and spanning a richness range $20 \leq \lambda \leq 230$. At the time this paper is being written, the observations of the galaxy clusters included in our sample have already been completed. No further galaxy spectroscopic redshifts will be assigned to these clusters during the final stages of the SDSS-IV program.

2.4 Interloper rejection

The observables on which the analysis is based are the galaxy projected clustercentric distance R and the rest-frame LOS velocity v_{rf} . We extract v_{rf} from the galaxy redshift z_{gal} and equivalent velocity $v(z_{\text{gal}})$ as $v_{\text{rf}} \equiv (v(z_{\text{gal}}) - v(z_c))/(1 + z_c)$, with z_c being the cluster redshift.

Even though the SPIDERS automated procedure assesses membership for each galaxy, there could still be interloper galaxies, i.e. galaxies that are projected inside the cluster virial region, but do not actually lie inside it. To reduce this contamination, we apply the ‘Clean’ method (Mamon et al. 2013), which uses the projected phase space location of each galaxy and its comparison to the expected maximal LOS velocity at each projected radius estimated for the cluster. Because we do not have enough spectroscopic redshifts to do this accurately for each individual cluster, we divide our sample into bins of richness and perform the interloper rejection in each of them separately. Specifically, we divide the sample into 15 equally spaced λ bins and build a composite cluster in each bin. We apply no scaling in velocity, and stack in physical radius [Mpc] to build the composite clusters.

The ‘Clean’ method is implemented through several steps. First, the cluster mass is estimated from the LOS velocity dispersion σ_{LOS} of each composite cluster, using a scaling relation calibrated using numerical simulations (e.g. Saro et al. 2013), and assuming an NFW (Navarro, Frenk and White) mass profile with concentration sampled from the theoretical mass–concentration relation of Macciò, Dutton & van den Bosch (2008). Thereafter, assuming the Mamon & Lokas (2005, M Λ) velocity anisotropy profile model, and given the $M(r)$ of the cluster, a Gaussian LOS velocity dispersion profile with $\sigma_{\text{LOS}}(R)$ is calculated and used to iteratively reject galaxies with $|v_{\text{rf}}| > 2.7\sigma_{\text{LOS}}$ at any clustercentric distance (see Mamon, Biviano & Murante 2010; Mamon et al. 2013). In Fig. 1, we show the location of galaxies in projected phase space with the identification of cluster member galaxies for the composite cluster constructed using those objects having richness in the range $20 \leq \lambda \leq 23.5$.

The distribution of the final sample of galaxies in projected phase space is presented in Fig. 2. In this plot, we show the galaxies identified as cluster members (red dots), the rejected interlopers (black dots), and the radial and velocity distributions of the member galaxies with measured redshifts (green histograms).

We also note that, even after carrying out interloper rejection, there is still a degree of contamination by interlopers. In fact, galaxies that lie outside the virial radius will tend to have smaller peculiar velocities than those galaxies lying within the virial region. Indeed, close to the cluster turnaround radius the galaxies will have negligible peculiar velocity and cannot be removed from the sample through an interloper rejection algorithm of the type we adopt here.

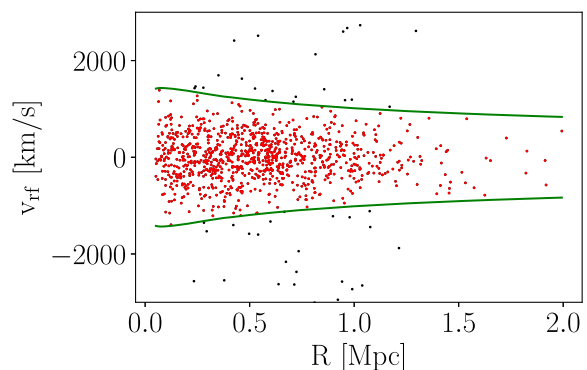


Figure 1. The projected phase space diagram for the composite cluster constructed using those objects having richness in the range $20 \leq \lambda \leq 23.5$. Green lines represent the radially dependent $2.7\sigma_{\text{LOS}}$ cut used to reject interlopers (indicated by black dots).

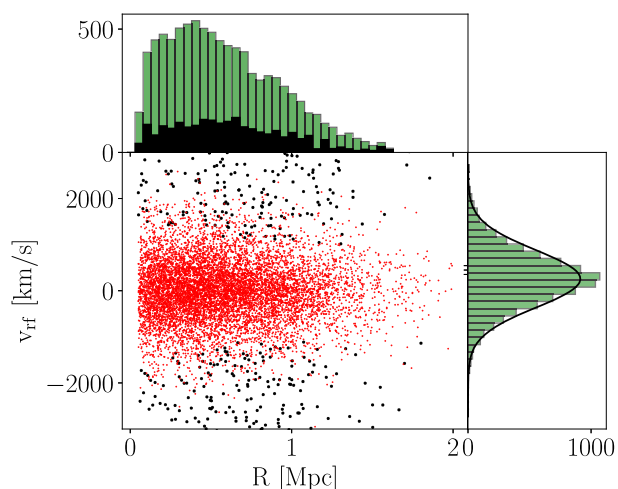


Figure 2. Projected phase space distribution for the final sample of 428 clusters. Red dots indicate the 7807 cluster members, while black dots mark the ~ 2000 rejected interloper galaxies. In the upper panel, we show in green the radial distribution of the member galaxies with measured redshifts, and in black the radial distribution of the interlopers. The panel on the right shows the distribution of rest-frame velocities, with an overlaid Gaussian of the same dispersion for comparison.

In fact there is no obvious method for separating these galaxies from the sample within the cluster virial region that we wish to model. An analysis of cosmological N -body simulations carried out by Saro et al. (2013) shows that, when passive galaxies are selected, this contamination is characteristically ~ 20 per cent for massive clusters ($M_{200c} \geq 10^{14} M_{\odot}$). For less-massive clusters, the contamination is expected to be higher. Another work carried out by Mamon et al. (2010), based on hydrodynamical cosmological simulations, showed that the distribution of interlopers in projected phase space is nearly universal, presenting only small trends with cluster mass. They state that, even after applying the iterative $2.7\sigma_{\text{LOS}}$ velocity cut, the fraction of interlopers is still 23 ± 1 per cent of all DM particles with projected radii within the virial radius, and over 60 per cent between 0.8 and 1 virial radius. Further exploration of the effects of this contamination on the dynamical analysis is required, and we are pursuing that in a separate study (Capasso et al., in preparation).

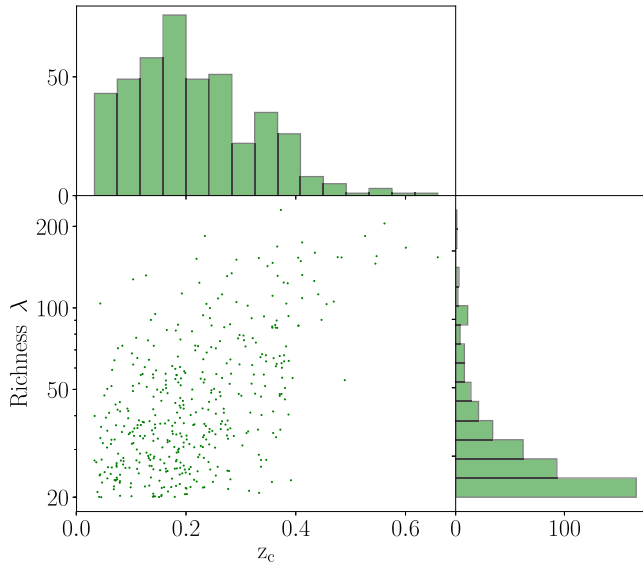


Figure 3. Distribution of richness λ and cluster redshift z_c of the final cluster sample.

After the application of the interloper rejection, we are left with a total of 703 clusters and 9121 red galaxies. For the analysis presented here we apply another cut on the cluster sample, keeping all CODEX systems that currently have at least 10 spectroscopic members, $N_{\text{mem}} \geq 10$. After this cut, our sample consists of 428 clusters and 7807 red galaxies, with a median redshift, richness, and luminosity of $z = 0.18$, $\lambda = 41$, and $L_X = 9.2 \times 10^{43} \text{erg s}^{-1}$, respectively. Fig. 3 shows the distributions of cluster redshift and richness of the final sample.

2.5 Galaxy number density profile

The Jeans analysis requires knowledge of the 3D number density profile $\nu(r)$ of the tracer populations whose dynamical properties are being used to study the mass and orbital properties of the system. In our case, these are the RS galaxies selected by the redMaPPer algorithm for observations within SPIDERS. As only the logarithmic derivative of $\nu(r)$ enters the Jeans equation (see equation 1), the absolute normalization of the galaxy number density profile has no impact on our analysis. However, a radially dependent incompleteness in the velocity sample would impact our analysis. In general, the spectroscopic followup within SPIDERS will lead to a radially dependent incompleteness. This means we cannot simply adopt the spectroscopic sample to measure the number density profile of the tracer population. We therefore rely on a study of the galaxy populations in 74 SZE-selected clusters from the SPT-SZ survey, which have been imaged as part of the DES Science Verification phase (Hennig et al. 2017). That study found no mass or redshift trends in the radial distribution of RS galaxies for $z > 0.25$ and $M_{200c} > 4 \times 10^{14} M_\odot$, finding the number density profile of the RS population to be well fitted by a NFW model (Navarro, Frenk & White 1996) out to radii of $4r_{200c}$, with a concentration for cluster galaxies of $c_{\text{gal}} = 5.37^{+0.27}_{-0.24}$. Therefore, we adopt the number density profile described by an NFW profile with the above-mentioned value of c_{gal} and a scale radius $r_{s, \text{gal}} = R_{200c}/c_{\text{gal}}$, making the assumption that the dynamical properties of our spectroscopic sample are consistent with the dynamical properties of the RS galaxy population used to measure the radial profiles.

We note that the Hennig et al. (2017) study indicates significant cluster to cluster scatter in the NFW concentration. We do not expect this scatter to be a source of significant bias in our analysis, because in an earlier analysis, Capasso et al. (2019) showed that the mean masses extracted from composite clusters and from the fitting of an ensemble of individual clusters are in good agreement. We will nevertheless further examine the impact of mismatch between the model and actual radial distribution of the tracer population in an upcoming study where we seek to improve the understanding of biases and scatter in dynamical mass estimators using mock observations of structure formation simulations (Capasso et al., in preparation).

3 THEORETICAL FRAMEWORK

The method we adopt for the dynamical analysis of our clusters is based on the spherically symmetric Jeans analysis (Binney & Tremaine 1987). Using the Jeans equation, it is possible to define the mass distribution $M(r)$ of a cluster as

$$\frac{GM(< r)}{r} = -\sigma_r^2 \left(\frac{d \ln \nu}{d \ln r} + \frac{d \ln \sigma_r^2}{d \ln r} + 2\beta \right), \quad (1)$$

where $\nu(r)$ is the number density profile of the tracer galaxy population, $\sigma_r(r)$ is the radially dependent component of the velocity dispersion along the spherical coordinate r , $M(< r)$ is the enclosed mass within radius r , G is Newton's constant, $\beta(r) \equiv 1 - (\sigma_\theta^2/\sigma_r^2)$ is the radially dependent velocity dispersion anisotropy, and σ_θ is the tangential component of the velocity dispersion. The observables we employ to constrain these quantities are projected quantities, including the surface density profile of the galaxy distribution, the rest-frame LOS velocities, and the radial separation of each galaxy from the cluster centre.

Given the limited knowledge of the LOS velocity distribution within realistic cluster dynamical data sets, it is not possible to uniquely derive the mass distribution of a galaxy cluster (Merritt 1987). To address this problem, we use the MAMPOSSt algorithm (for full details please refer to Mamon et al. 2013). This code performs a maximum likelihood analysis of the projected phase space distribution of the observed sample using the theoretical distribution predicted for a given model using the Jeans equation. The observations are used to constrain the model parameters adopted to describe the cluster mass distribution and galaxy orbital anisotropy. The MAMPOSSt method thus requires adopting parametrized models for the number density, mass, and velocity anisotropy profiles $\nu(r)$, $M(r)$, and $\beta(r)$. As addressed in Section 2.5, because our spectroscopic data set might suffer from radially dependent incompleteness, we adopt the measured number density profile derived from the study of RS galaxies in SZE-selected clusters (Hennig et al. 2017). We discuss our choice of the mass and velocity anisotropy profiles in the next section.

3.1 Mass and anisotropy profiles

Taking guidance from both numerical studies of structure formation and observational results, we adopt the mass model introduced by Navarro et al. (1996, NFW)

$$\rho(r) = \rho_0 \left(\frac{r}{r_s} \right)^{-1} \left(1 + \frac{r}{r_s} \right)^{-2}, \quad (2)$$

where ρ_0 is the central density, and r_s is the scale radius where the logarithmic derivative of the density profile reaches -2 . Integrating

this density profile up to r_{200c} , we obtain the mass enclosed inside the virial radius

$$M_{200c} = 4\pi\rho_0 r_s^3 \left[\ln \left(\frac{r_s + r_{200c}}{r_s} \right) - \frac{r_{200c}}{r_s + r_{200c}} \right]. \quad (3)$$

Cosmological simulations produce DM haloes with mass profiles well described by this profile. Even though some results have preferred different models (Merritt et al. 2006; Navarro et al. 2010; Dutton & Macciò 2014; van der Burg et al. 2015; Sereno & Ettori 2017), this result is in good agreement with a variety of observational analyses using both dynamics and weak lensing (Carlberg et al. 1997; van der Marel et al. 2000; Biviano & Girardi 2003; Katgert, Biviano & Mazure 2004; Umetsu et al. 2011).

For the velocity anisotropy profile, we consider five models that have been used in previous MAMPOSSt analyses and that are described also in Capasso et al. (2019). These are (1) the constant anisotropy model (C), (2) the Tiert anisotropy profile (Tiert et al. 2007, T), (3) the Mamon & Łokas (2005) profile (MŁ), (4) the Osipkov–Merritt anisotropy profile (Osipkov 1979; Merritt 1985, OM), and (5) a model with anisotropy of opposite sign at the centre and at large radii (O).

Therefore, to predict the projected phase space distribution of the observed dynamical data set for each cluster, we run MAMPOSSt with three free parameters: the virial radius r_{200c} , the scale radius r_s of the mass distribution, and a velocity anisotropy parameter θ_β . This parameter represents the usual $\beta = 1 - (\sigma_\theta^2/\sigma_r^2)$ for the first three models (C, T, and O), while for the MŁ and OM models it defines a characteristic radius $\theta_\beta = r_\beta$.

3.2 Bayesian model averaging

As the literature does not provide us with strong predictions for the radial form of the velocity anisotropy profile $\beta(r)$, we employ all the five models described above when estimating the cluster masses. We combine the results from the different models by merging their constraints exploiting the Bayesian model averaging technique. A weight is assigned to each model, which is proportional to how well the model fits the data. This weight is represented by the so-called Bayes factor (see Hoeting et al. 1999, and references therein).

Considering the five anisotropy models M_1, \dots, M_5 , we define the Bayes factor B_j of each model j by normalizing the marginalized likelihood of the model $\mathcal{L}(D|M_j)$, also known as evidence, by the likelihood of the most probable model. Specifically,

$$B_j = \frac{\mathcal{L}(D|M_j)}{\mathcal{L}(D|M_{\max})}, \quad (4)$$

where M_{\max} indicates the model with the highest marginalized likelihood, $\mathcal{L}(D|M_j) = \int \mathcal{L}(D|\theta_j, M_j)P(\theta_j|M_j) d\theta_j$, $\mathcal{L}(D|\theta_j, M_j)$ is the likelihood of the data D given the model parameters θ_j , and $P(\theta_j|M_j)$ is the prior.

The average posterior distribution on the parameter common to all anisotropy models is then simply given by the weighted average of the posterior distributions of each model, with the Bayes factor as weight. To perform this Bayesian model averaging, we employ the multimodal nested sampling algorithm MULTINEST (Feroz & Hobson 2008; Feroz, Hobson & Bridges 2009; Feroz et al. 2013), which provides us with the evidence for each model.

4 RESULTS

In this section, we present the results of our dynamical analysis. In the first subsection, we describe how we calibrate the λ –mass

Table 1. Priors assumed for our analysis. $\mathcal{U}(i, j)$ refers to a uniform flat prior in the interval (i, j) , while $\mathcal{N}(\mu, \sigma^2)$ indicates a Gaussian distribution with mean μ and variance σ^2 .

A_λ	B_λ	γ_λ	r_β	$\sigma_{\ln\lambda}^{\text{int}}$
$\mathcal{U}(20, 50)$	$\mathcal{U}(0.5, 2)$	$\mathcal{U}(-3, 2)$	$\mathcal{U}(0.01, 10)$	$\mathcal{N}(0.15, 0.09^2)$

relation and present our results. In the following subsection, we explore the impact of correlated scatter in the X-ray luminosity and richness for the CODEX sample. Afterwards, we compare our findings to previous works, and we test how strongly the number of member galaxies per cluster affects our results.

4.1 λ – M_{200c} – z relation

We adopt a power-law relation between cluster richness λ , mass, and redshift of the form

$$\lambda = A_\lambda \left(\frac{M_{200c}}{M_{\text{piv}}} \right)^{B_\lambda} \left(\frac{1+z}{1+z_{\text{piv}}} \right)^{\gamma_\lambda}, \quad (5)$$

where A_λ , B_λ , and γ_λ are the amplitude, the mass slope, and the redshift evolution slope. Similar forms have been used to study the galaxy halo occupation number and richness previously (Lin, Mohr & Stanford 2004; Lin et al. 2006; Saro et al. 2015; Hennig et al. 2017; Saro et al. 2017). We adopt the redshift scaling $(1+z)^\gamma$ instead of $E(z)^\gamma$ because, as discussed in a recent study of X-ray scaling relations (Bulbul et al. 2018), we wish to avoid ascribing cosmological sensitivity to redshift trends unless there is a physically justifiable reason to do so. Sensitivity of an observable to the evolving critical density of the Universe would justify an $E(z)$ scaling. An example would be an observable like the X-ray luminosity or SZE signature that depends on the ICM density, but in the case of the galaxy richness or halo occupation number, the density plays no role and no such sensitivity is expected. We set the pivot redshift to be $z_{\text{piv}} = 0.18$, which is the median redshift of our cluster sample. We have adjusted the value of the mass pivot $M_{\text{piv}} = 3 \times 10^{14} M_\odot$ iteratively to minimize the false degeneracy between A_λ and B_λ .

We marginalize over the intrinsic scatter in λ at fixed mass, which is set to be lognormal with a prior on the scatter from Saro et al. (2017), $\sigma_{\ln\lambda}^{\text{int}} = 0.15 \pm 0.09$ (precise priors listed in Table 1). We assume the full scatter in λ at fixed mass is lognormal with variance given by:

$$\sigma_{\ln\lambda}^2 = \frac{\eta}{\lambda} + \sigma_{\ln\lambda}^{\text{int}^2}, \quad (6)$$

where η is the scale factor described in Section 2.2 that is a correction factor that accounts for the limited depth of the SDSS photometry in accounting for the richness calculated over a fixed portion of the cluster galaxy luminosity function.

For each cluster i in our sample, we calculate an initial mass $M_{200c, \text{obs}}$ using the scaling relation described in equation (5) and the current values of the parameter vector \mathbf{p} , which contains the four scaling relation parameters A_λ , B_λ , γ_λ , and $\sigma_{\ln\lambda}^{\text{int}}$ together with the anisotropy model parameter r_β . In each iteration, we use the current value of the scatter $\sigma_{\ln\lambda}$ to estimate a correction for the Eddington bias caused by the interplay of the λ scatter and the mass function using the method described in Mortonson, Hu & Huterer (2011). Assuming a lognormal mass observable relation with variance $\sigma_{\ln M}^2 = (1/B_\lambda \cdot \sigma_{\ln\lambda})^2$ that is small compared with the scale over which the local slope Γ of the mass function changes, the

Table 2. RedMaPPer richness–mass–redshift scaling relation parameters from this analysis and the literature. The results from our analysis include corrections for the Eddington and Malmquist biases. Parameters are defined in equation (5). For results from this analysis, the uncertainties are statistical, and a systematic mass uncertainty of 10 per cent is applied to the amplitude A_λ . In the comparison to previous results, the amplitude A_λ column contains the λ at $M_{200c} = 3 \times 10^{14} M_\odot$ and $z = 0.18$. Conversions have been made to M_{200c} and from $E(z)$ to $(1+z)$ where needed. Note also that each of these studies was performed on a different range of mass and redshift.

Dynamical analyses using SPIDERS data	A_λ	B_λ	γ_λ
Baseline analysis: $\lambda \geq 20$, $N_{\text{mem}} \geq 10$	$38.6^{+3.1}_{-4.1} \pm 3.9$	$0.99^{+0.06}_{-0.07} \pm 0.04$	$-1.13^{+0.32}_{-0.34} \pm 0.49$
As above, but with correlated scatter correction	$39.8^{+3.0}_{-3.8} \pm 4.0$	$0.98^{+0.07}_{-0.07} \pm 0.04$	$-1.08^{+0.31}_{-0.34} \pm 0.49$
Previously published results	$\lambda(3 \times 10^{14} M_\odot, 0.18)$	$M_{200c}^{B_\lambda}$	$(1+z)^{\gamma_\lambda}$
WL masses using DES Y1 (McClintock et al. 2018)	43.8 ± 1.3	0.73 ± 0.03	-0.10 ± 0.10
CMB WL masses (Baxter et al. 2018)	49.8 ± 10.8	0.81 ± 0.21	–
WL masses using SDSS (Simet et al. 2017)	63.1 ± 2.2	0.74 ± 0.06	–
Cluster clustering using SDSS (Baxter et al. 2016)	37.5 ± 4.4	0.84 ± 0.12	0.70 ± 0.90
Pairwise velocity dispersion with SDSS (Farahi et al. 2016)	47.7 ± 1.0	0.75 ± 0.04	–
SPT masses with RM from DES SV (Saro et al. 2015)	36.1 ± 9.1	1.16 ± 0.20	0.60 ± 0.63

posterior mass distribution is a lognormal of the same variance $\sigma_{\ln M}^2$ with a shifted mean $\ln \langle M_{200c, \text{true}} \rangle = \ln \langle M_{200c, \text{obs}} \rangle + \Gamma \sigma_{\ln M}^2$.

With this mass, we then use MAMPOSSt to construct the probability distribution in projected phase space for each cluster, combining the likelihoods calculated for each member galaxy in that cluster

$$\mathcal{L}_i = \prod_{j \in \text{gal}} \mathcal{L}(R^j, v_{\text{rf}}^j, \lambda_i, z_i | \mathbf{p}), \quad (7)$$

where R^j and v_{rf}^j are the clustercentric radii and rest-frame velocities of the member galaxy j in the cluster i . The maximum-likelihood solutions are obtained using the NEWUOA software (Powell 2006). Flat priors are assumed for the scaling relation parameters A_λ , B_λ , and γ_λ , and for the anisotropy parameter r_β (see Table 1).

We combine the likelihoods for all these clusters, to then obtain the likelihood for the total sample for each set of scaling relation parameters \mathbf{p} , i.e. $\mathcal{L} = \prod_{i \in \text{clus}} \mathcal{L}_i$. This procedure must be done separately for each anisotropy profile model (see Section 3.1). Finally, we use Bayesian model averaging to combine the posterior parameter distributions obtained from the different anisotropy models, effectively marginalizing over the uncertainties in the orbital anisotropy.

Because we impose a cut on our observable, $\lambda \geq 20$, a correction for the Malmquist bias is also needed (Sandage 2000). We estimate the effect of this correction by creating a large mock catalogue (~ 4400 clusters and $\sim 165\,500$ member galaxies) by computing the number of expected clusters as a function of halo mass and redshift using the halo mass function (Tinker et al. 2008). We then draw a Poisson realization of the number of expected clusters, obtaining a mass-selected cluster sample with $M_{200c} \geq 7 \times 10^{13}$ and $0.05 \leq z \leq 0.66$. Using the scaling relation parameters recovered from our analysis before correcting for this bias, we calculate λ for each cluster of mass M_{200c} . Scatter is added to this relation such that the assigned λ values are sampled from a Gaussian distribution having scatter given by equation (6). The mock sample we produce has richnesses $\lambda > 6.5$. For each cluster in our mock sample, we create a sample of member galaxies. We run MAMPOSSt on a grid of velocities and clustercentric distances, fixing the galaxy number density profile to that described in Section 2.5, and generating a random number of galaxies per cluster drawn from the distribution of member galaxies in our observed sample. Finally, we use the MAMPOSSt likelihood to recover the probability density

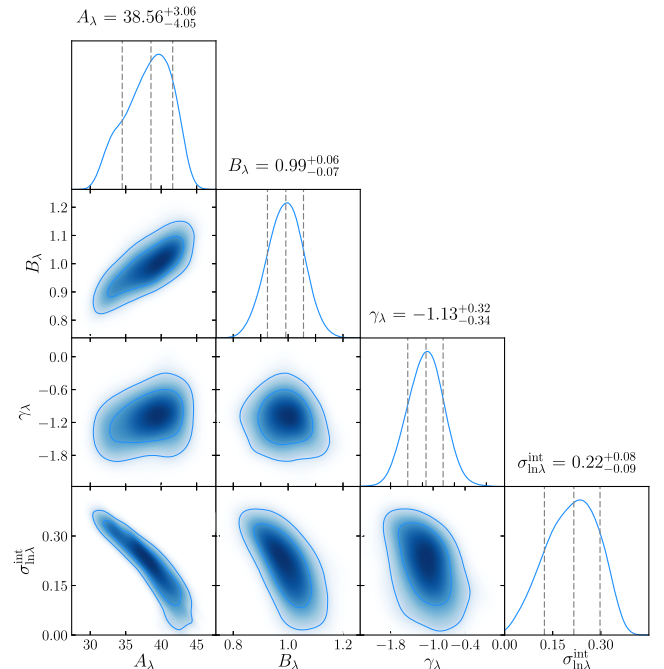


Figure 4. Parameters of the λ – M_{200c} – z relation. Contours show the 1 σ , 2 σ , and 3 σ confidence regions.

of observing an object at a certain location in phase space (see equation 11, Mamon et al. 2013).

We fit this mock data set and recover best-fitting parameter values that are consistent with the input values. Then, we impose a $\lambda > 20$ richness cut on the sample and refit, noting that the best-fitting mass and redshift trends are affected. Using this approach, we estimate corrections for the Malmquist bias that correspond to $\delta B_\lambda = +0.05$ and $\delta \gamma_\lambda = -0.06$. These corrections are included in all the results we present.

Table 2 summarizes the posterior of our model parameters from our so-called ‘baseline analysis’, i.e. before accounting for the impact of correlated scatter (see Section 4.2.2), while Fig. 4 shows the corresponding joint parameter constraints. Our results imply that galaxy clusters with redshift $z = 0.18$ and mass $M_{200c} = 3 \times 10^{14} M_\odot$ have a mean richness of $A_\lambda = 38.56^{+3.06}_{-4.05}$. The mass

Table 3. Impact of the number of spectroscopic members on the redMaPPer richness–mass–redshift scaling relation parameters. Parameters are defined in equation (5). The uncertainties on the results are statistical, corresponding to 68 per cent confidence intervals, and a systematic mass uncertainty of 10 per cent is applied to the amplitude A_λ .

Number of cluster member galaxies	A_λ	B_λ	γ_λ
$N_{\text{mem}} \geq 1$	$39.2^{+2.9}_{-3.5}$	$0.91^{+0.05}_{-0.06}$	$-0.15^{+0.23}_{-0.24}$
$N_{\text{mem}} \geq 3$	$39.3^{+3.1}_{-3.6}$	$0.92^{+0.05}_{-0.06}$	$-0.26^{+0.23}_{-0.24}$
$N_{\text{mem}} \geq 5$	$39.2^{+3.0}_{-3.7}$	$0.95^{+0.06}_{-0.06}$	$-0.65^{+0.26}_{-0.27}$
$N_{\text{mem}} \geq 10$	$38.6^{+3.1}_{-4.1}$	$0.99^{+0.06}_{-0.07}$	$-1.13^{+0.32}_{-0.34}$
$N_{\text{mem}} \geq 20$	$41.6^{+2.5}_{-3.2}$	$0.98^{+0.09}_{-0.08}$	$-1.00^{+0.49}_{-0.56}$

scaling is consistent with linear, $B_\lambda = 0.99^{+0.06}_{-0.07}$. The redshift dependence in the CODEX sample is $\gamma_\lambda = -1.13^{+0.32}_{-0.34}$, indicating that the RS richness λ at fixed mass falls as one moves to higher redshift.

4.2 Additional systematic effects

The results presented in the last section include corrections for the Eddington bias and the Malmquist bias, but the uncertainties on the parameters reflect only statistical errors. In this section, we consider systematic effects and the impact they have on the best fit parameters and the parameter uncertainties.

We estimate that there is an additional 10 per cent systematic uncertainty associated with the dynamical mass measurements themselves. This estimate comes from an analysis of the MAM-POSS code run on numerical simulations in the analysis of Mamon et al. (2013). In their work, the authors show that, using particles lying within a sphere of r_{100} around the halo centre, the estimate of the cluster virial radius r_{200c} is biased at ≤ 3.3 per cent (see Table 2, Mamon et al. 2013). Therefore, we adopt a Gaussian systematic uncertainty on the virial mass M_{200c} of $\sigma = 10$ per cent. The Mamon et al. (2013) analysis does not explore mass or redshift trends in these biases, and therefore we apply the entire uncertainty to the normalization parameter A_λ . In a future analysis, we plan to explore the mass and redshift dependence of the systematic uncertainties in dynamical mass estimates from a Jeans analysis (Capasso et al., in preparation).

In the subsections below, we first consider the impact of selecting different subsamples using the number of member galaxies with spectroscopic redshifts N_{mem} , and then we explore the impact of possible correlated optical and X-ray scatter.

4.2.1 Impact of number of cluster member galaxies

As described in Section 2.3.2, we apply a cut to our sample prior to the dynamical analysis, keeping only those systems having at least 10 spectroscopic members: $N_{\text{mem}} \geq 10$. This decision is driven by our concern that good constraints on the cluster masses and scaling relation parameters could not be obtained from clusters having very small numbers of spectroscopic members. However, this selection is somewhat arbitrary, and so we explore here the impact of varying this cut.

Table 3 shows the results obtained imposing different cuts on the number of spectroscopic members, where N_{mem} varies from 1 to 20. Note that the BCG has been excluded, so the clusters with a single galaxy actually have two measured redshifts. Interestingly,

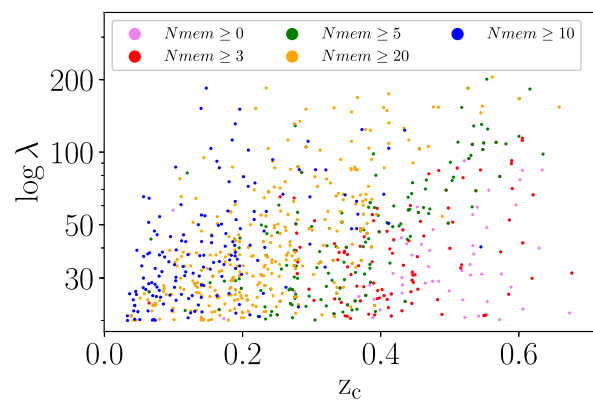


Figure 5. Richness and redshift distribution of clusters having a different number of spectroscopic members.

the normalization A_λ and the mass trend parameter B_λ are not significantly affected when analysing clusters having a different number of spectroscopic members.

On the other hand, the value of the redshift trend parameter γ_λ varies considerably, even reaching values consistent with zero evolution when including clusters having $N_{\text{mem}} \geq 1$ and ≥ 3 . The value of γ_λ becomes stable when including only clusters with at least 10 spectroscopic members, justifying our decision of including only those clusters into our main analysis. However the strong dependence of γ_λ on the member cut is an indication of remaining systematic uncertainties on this parameter.

The reason of the different behaviour of γ_λ with respect to that of A_λ and B_λ is clarified to some degree in Fig. 5, where we show the distribution in richness and redshift of galaxy clusters having a different number of spectroscopic members. The distribution of clusters having $N_{\text{mem}} < 10$ extends to higher redshifts, allowing for improved constraints on the redshift trend and also introducing a qualitatively different population of clusters into the analysis.

As the spectroscopic sample at these higher redshifts is increased, we will begin to see whether the trend in γ_λ with the N_{mem} cut is revealing a systematic in dynamical masses in the limit of very low spectroscopic sampling of each halo or whether the weaker trends shown with the less dramatic cuts that then include more high-redshift systems is really a reflection of the true redshift trend in the λ –mass relation. But at this point we use the trend in γ_λ that is apparent in Table 3 to estimate a systematic uncertainty on that parameter. Specifically, we adopt half the full range of variation in the value as the systematic uncertainty on the parameter $\sigma_{\text{sys}, \gamma_\lambda} = \frac{\Delta|\gamma_\lambda|}{2} = 0.49$. Similarly for the mass trend parameter, we estimate $\sigma_{\text{sys}, B_\lambda} = \frac{\Delta|B_\lambda|}{2} = 0.035$. For the amplitude parameter A_λ , the shift is small compared to the 10 per cent systematic uncertainty described at the beginning of this section. These systematic uncertainties are listed in Table 2.

4.2.2 Impact of correlated λ and L_X scatter

Before comparing our results to those from the literature, we examine the impact of correlated scatter in the richness and X-ray luminosity on the parameters of the richness–mass relation. To do this, we employ the selection function of the CODEX survey calculated as described below by the CODEX team.

As described above in Section 2.2, the CODEX cluster catalogue is based on the identification of faint X-ray sources with the help of redMaPPer follow-up on the SDSS photometry to identify optical

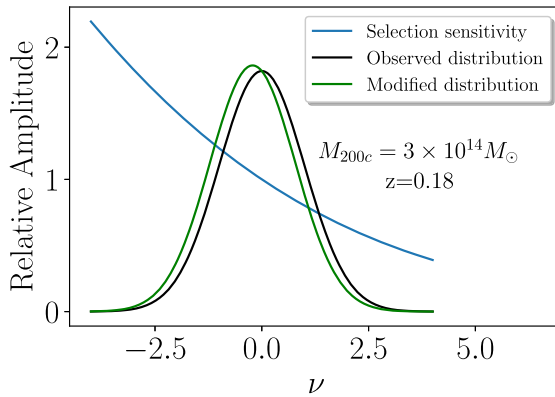


Figure 6. Effect of the selection function on the λ distribution. In blue, we show the relative sensitivity of the CODEX X-ray-selected sample as a function of deviation from the mean observed λ , normalized to its value at $\nu = 0$. The black curve shows the distribution of observed λ , as a function of deviation ν from the mean value, while the green distribution shows how the inclusion of the selection sensitivity causes a shift and distortion of the observed λ distribution.

counterparts. The final catalogue is therefore subject to both X-ray and optical selection in a manner that has been modelled based upon several observational results. First, the LoCuSS survey (Local Cluster Substructure Survey, Okabe et al. 2010; Haines et al. 2018) indicates a negative value of the covariance at fixed mass of the scatter in the X-ray luminosity L_X and the optical richness λ . For the selection function modelling adopted here, the covariance coefficient is fixed to be $\rho_{L_X-\lambda} = -0.2$ (Farahi et al. in preparation). The net effect of this correlated scatter is that the CODEX survey is more sensitive in detecting clusters of given mass if they have lower richness, because that lower richness is correlated to a higher X-ray luminosity. The modelling of the survey selection function takes into account the covariance of the scatter in L_X –mass relation with the shape of the cluster, which affects the sensitivity to a particular cluster. In modelling the selection function, the scaling relations are fixed to those of the XXL survey (e.g. Pacaud et al. 2016), which is well suited for our study here, because it includes both cluster and group mass scales.

Using the selection function described above, the CODEX team then estimated the effective solid angle of the CODEX survey as a function of the scatter in λ as a function of redshift and mass. The idea here is that because scatter to lower λ is weakly correlated to an increase in the cluster X-ray luminosity, one is effectively probing a larger solid angle for those clusters with lower than typical λ at each redshift and mass. It is with this data product that we begin our analysis.

To estimate the impact of this correlated scatter on our results, we calculate its effects a posteriori, using the results of our baseline analysis as listed in Table 2. The variation in sensitivity as a function of λ at fixed mass and redshift produces a modification in the shape of the richness distribution at each mass and redshift. In Fig. 6, we show an example of how this affects the cluster distribution in λ at $M_{200c} = 3 \times 10^{14} M_\odot$ and $z = 0.18$. The blue line represents the relative sensitivity $s(\nu)$ of the CODEX X-ray-selected sample as a function of the deviation ν from the mean, expected λ (expressed in equation 5). This deviation is defined as a function of

$$\nu = \frac{\Delta \ln \lambda}{\sigma_{\ln \lambda}^{\text{int}}}, \quad (8)$$

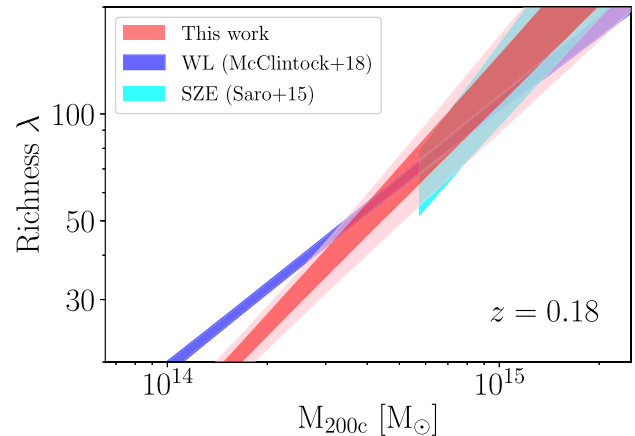


Figure 7. Best-fitting model for our richness–mass relation (in red), evaluated at the redshift $z = 0.18$, compared to other measurements. For our analysis, we also show the 2σ confidence area (pink region around the red relation). Confidence regions include statistical uncertainties only.

and the sensitivity function has been normalized to its value at $\nu = 0$. The black curve shows the lognormal parent distribution of λ at this mass and redshift (equation 6), as a function of the deviate ν . In this space, this distribution is simply a Gaussian of unit width. The green distribution shows the product of the parent λ distribution with the selection sensitivity. Given the ν dependence of the sensitivity, the new λ distribution is well approximated as being a new lognormal distribution with mean shifted away from zero. The shift in the parent λ distribution can be written

$$\langle \nu | M_{200c}, z \rangle = \int d\nu P(\nu) s(\nu | M_{200c}, z). \quad (9)$$

where $P(\nu)$ is the parent λ distribution (lognormal) and $s(\nu | M_{200c}, z)$ is the sensitivity as a function of ν given the cluster mass and redshift. For the given example, the mean shift is $\langle \nu | M_{200c}, z \rangle = -0.20$. This shift changes little with mass, but it does evolve with redshift. This fractional logarithmic shift then implies a shift in λ for any given mass and redshift

$$\lambda_{\text{cor}} = \lambda(M_{200c}, z) e^{-(\nu | M_{200c}, z) \sigma_{\ln \lambda}} \quad (10)$$

To estimate the impact on the scaling relation parameters, we calculate λ_{cor} over the full range of M_{200c} , z where we have clusters. Using these results, we fit a scaling relation of the same form as equation (5) to the corrected data. Table 2 contains the best-fitting parameters and 1σ uncertainties of the λ –mass relation with the correlated scatter correction. The impact of the correlated scatter in λ and L_X is smaller than the 1σ statistical parameter uncertainty for all three parameters. Thus, for a sample the size of the current SPIDERS analysis, this effect can be safely ignored.

4.3 Comparison to previous results

In this section, we compare our calibration of the richness–mass relation to previous results from the literature. We show the mass and redshift trends of λ in Figs 7 and 8, respectively, where for the redshift trend we correct the data points to the mass $M_{200c} = 3 \times 10^{14} M_\odot$ and for the mass trend we move the data points to the redshift $z = 0.18$. These are the mass and redshift pivots of our sample, and are therefore the places where our constraints are tightest. The best-fitting model for the λ – M_{200c} relation is shown in red, with shaded 1σ and 2σ confidence regions. For the results

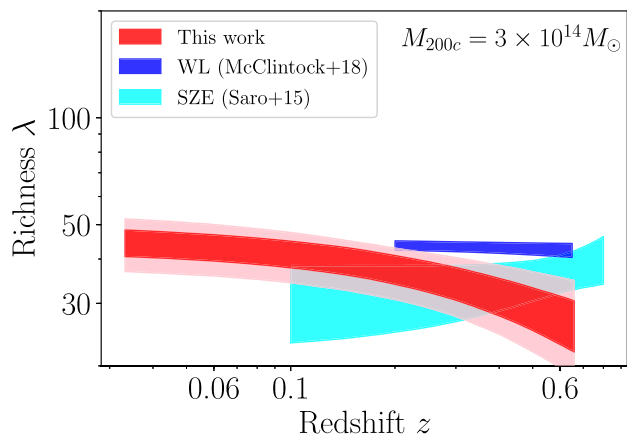


Figure 8. Best-fitting model for our richness–redshift relation (in red), evaluated at our pivot mass $M_{\text{piv}} = 3 \times 10^{14} M_{\odot}$, compared to previous works. For our analysis, we also show the 2σ confidence region. Confidence regions include statistical uncertainties only.

from Saro et al. (2015, in cyan) and McClintock et al. (2018, in blue), we show only the 1σ confidence region. We limit the redshift range to that analysed in each work. Fig. 7 makes clear that the mass slope of our relation lies in between that of Saro et al. (2015) and McClintock et al. (2018). In Fig. 8, our results suggest stronger negative redshift evolution than in either previous results.

Table 2 lists the parameter estimates and uncertainties for all the comparison results. To make these comparisons, we scale all the measurements from previous analyses to the redshift $z_{\text{piv}} = 0.18$ (Fig. 7), and mass $M_{\text{piv}} = 3 \times 10^{14} M_{\odot}$ (Fig. 8), using the best-fitting redshift and mass trends published for each sample. Doing this, we predict the $\lambda(3 \times 10^{14} M_{\odot}, 0.18)$ for each previous work. All mass conversions needed for the comparison plot are carried out using COLOSSUS, an open-source PYTHON package for calculations related to cosmology (Diemer 2017). The mass and redshift trend parameters presented in Table 2 were also converted to those defined in equation (5) using the appropriate mass definition M_{200c} and redshift trend function $(1+z)^{\gamma_{\lambda}}$ adopted for our analysis here. In some cases, this involved inversions of the mass–observable relations.

Importantly, the definition of the cluster richness λ from the redMaPPer algorithm may differ from one data set to another. Before comparing to our results, we implement this correction using the conversion obtained by McClintock et al. (2018):

$$\begin{aligned} \lambda_{\text{DES SV}} &= (1.08 \pm 0.16) \lambda_{\text{DES Y1}} \\ \lambda_{\text{SDSS}} &= (0.93 \pm 0.14) \lambda_{\text{DES Y1}} \end{aligned} \quad (11)$$

where the number presented as the uncertainty is actually the standard deviation in the richness ratio (thus, the uncertainty on the mean conversion factor is tiny in comparison). We have applied these corrections to bring all results to the space of our analysis.

4.3.1 Discussion of the mass trend parameter B_{λ}

Our mass trend shows good agreement with the results obtained by Saro et al. (2015), which is based on measurements of a cross-matched sample of SZE-selected galaxy cluster candidates from the SPT 2500 deg² SPT–SZ survey and the optically selected redMaPPer clusters from the DES–SV data. We also find good agreement with the scaling relation obtained by Baxter et al. (2016,

2018), where the first is based on cluster clustering using SDSS data, and the second on CMB lensing measurements from SPT in combination with DES Y1 redMaPPer clusters.

On the other hand, our results are in disagreement with those of Simet et al. (2017), based on redMaPPer clusters found in the SDSS, and of McClintock et al. (2018), obtained analysing redMaPPer galaxy clusters identified in the DES Y1 data. While our analysis is performed on ensembles consisting of single clusters, these two analyses made use of stacked weak lensing data. In fact, neither of these analyses aimed to account for the Eddington bias and, therefore, they do not solve for the underlying richness–mass relation as we have done. Rather, they fit the mean λ within bins of λ and redshift to the mean weak lensing mass associated with each bin. Because the Eddington bias is a function of the scatter in λ and the effective slope of the mass function at the corresponding mass, ignoring the Eddington bias correction will lead to systematic errors in the redshift and mass trends. We estimate that the Eddington bias correction will impact the mass and redshift trends with $\delta B_{\lambda} = +0.04$ and $\delta \gamma_{\lambda} = +0.09$, respectively, where δ is defined as the value of the parameter after applying the bias correction minus the one before the correction. With these corrections, the expected parameters for the underlying λ –mass relation would be $B_{\lambda} = 0.77$ and $\gamma_{\lambda} = -0.01$. These are still offset significantly from our measured values at $\Delta B_{\lambda} = -0.21 \pm 0.08$ (2.7σ) and $\Delta \gamma_{\lambda} = +1.12 \pm 0.60$ (1.9σ), and so clearly the Eddington bias is not large enough to explain the differences between the results.

We note that redMaPPer optical selection and RASS X-ray selection followed by cross-matching to redMaPPer (i.e. the CODEX sample we analyse here) will not generally lead to similar levels of sample contamination. Moreover, contamination would be expected to have a different impact on a stacked weak lensing analysis than on a cluster-by-cluster dynamical analysis like that carried out here. Thus, in principle, differences in the λ –mass relations constrained from these two different approaches can be used to shed light on the differences in contamination.

The contamination of optically selected cluster samples by projected collections of passive galaxies in low-mass groups and isolated systems has long been a concern (Gladders et al. 2007; Song et al. 2012; Costanzi et al. 2018), with estimates of contamination fractions reaching as high as ~ 50 percent. Within X-ray imaging surveys like those employing pointed ROSAT Position Sensitive Proportional Counter (PSPC) observations with ~ 25 arcsec full width at half-maximum imaging (e.g. Vikhlinin et al. 1998; Clerc et al. 2018), the selection of X-ray sources exhibiting extended emission has been shown to deliver contamination at the ~ 10 per cent level. Within the lower quality RASS imaging, where there is generally no extent information for the faint CODEX sources, the contamination is driven by random superpositions between the faint X-ray sources [~ 90 percent are active galactic nucleus (AGN) or stars] and the ubiquitous RS optical candidate clusters identified by redMaPPer (see detailed discussion of this problem and the description of a method to control this contamination in Klein et al. 2018, 2019).

Within a stacked weak lensing analysis, these contaminating low-mass systems would likely suppress the mass at a given λ , and a mass-dependent contamination that increases toward low λ , as suggested by some studies (Saro et al. 2015), could lead to a significant bias to low values in the mass slope B_{λ} . Within this context, it is interesting to note that the disagreement in the λ –mass relations between McClintock et al. (2018) and our analysis is largest at low λ .

For the CODEX sample, the random superpositions are not necessarily contaminants in a study of the λ -mass relation, because many of these random superpositions are of X-ray AGN projected to lie near true RS clusters on the sky. Subsequent spectroscopic follow-up of these systems, whether the X-ray emission is AGN or cluster dominated, leads to dynamical sampling of clusters and groups, with less impact from the tail of low-mass, contaminating structure projections than in the case of the purely optically selected sample. Spectroscopic followup further reduces the contamination, because those systems that are loose projections can in many cases be separated out from the true, collapsed haloes during the SPIDERS validation procedure (see also detailed spectroscopic studies of redMaPPer systems in Sohn et al. 2018; Rines et al. 2018).

Because our dynamical analysis uses (weak) mass information from all individual systems, the impact of the final remaining contamination in the CODEX calibration of the λ -mass relation, which would tend to be sampled with smaller numbers of spectroscopic redshifts, would then be further reduced. Thus, because both methods – optical cluster selection + stacked weak lensing and RASS+optical redMaPPer + dynamics – are subject to different systematic effects, we have a potential explanation for the different mass slopes observed in the two analyses. Further work using structure formation simulations or generation of realistic mocks including the appropriate contamination effects would be required to quantify these effects and understand the differences in detail. Supplementing this with dense spectroscopic studies of redMaPPer samples to better understand the nature of the projection and contamination issues will also be very helpful (Sohn et al. 2018; Rines et al. 2018).

Finally, we compare our scaling relation amplitudes and mass trends with those obtained by two recent low-redshift ($z \leq 0.33$) SDSS-based analyses. Murata et al. (2018) perform a richness–mass scaling relation calibration using a joint measurement of the abundance and stacked cluster weak lensing profiles within the context of the cosmological parameters preferred by *Planck* CMB anisotropy (Planck Collaboration et al. 2016). They determine a scaling relation that reproduces both the cluster counts and the lensing profiles but only at very large richness scatter $\sigma_{\ln \lambda|M} = 0.46$. Scatter of this scale predicts a non-negligible contribution of low-mass haloes ($M_{200m} \lesssim 10^{13} M_{\odot}$) in the SDSS redMaPPer sample. Their interpretation is that this contamination could be due to projection effects that preferentially impact the low richness portion of the sample ($20 \leq \lambda \leq 30$) or that the assumed *Planck* cosmology is different from the true underlying cosmology. We find good agreement with the mass trend of their results, but their amplitude is only about half of the value we find. The offsets in amplitude are not surprising given the very large differences in the scatter in the two analyses.

Jimeno et al. (2017) calibrate the mass–richness scaling relation using both the cluster correlation function and the cluster counts. They employ the *N*-body Millennium XXL simulations, updated to the *Planck* cosmology (Planck Collaboration et al. 2016) to predict the distributions of clusters in richness. They first obtain two independent mass–richness relations using separately clustering and counts data, and afterwards perform a joint analysis. Interestingly, they find a 2.5σ tension between the amplitudes of the scaling relation in the two cases that weakens if they shift from the *Planck* cosmological parameters to those from the *WMAP* mission (Spergel et al. 2003). The joint constraints on the amplitude and mass trend of the mass–richness relation are in good agreement with our results.

Overall, the agreement with the counts+clustering analysis is encouraging, suggesting that their modeling of the redMaPPer

selection and contamination cannot be far off. However, the counts + stacked weak lensing analysis seems to provide further indications that projection effects in the redMaPPer sample may be responsible for differences between stacked weak lensing constraints and measurements of the true underlying richness–mass relation from direct mass measurements (our analysis), from counts or from cluster clustering. Commonalities between the impact of correlated large-scale structure on weak lensing and richness measurements may lie at the heart of these differences.

4.3.2 Discussion of the redshift trend parameter γ_{λ}

Our constraint on the redshift trend of the λ - M_{200c} - z relation shows a stronger negative trend $\gamma_{\lambda} = -1.13 \pm 0.33 \pm 0.49$ than found in previous analyses (Fig. 8), which have provided no significant evidence of a redshift trend (Saro et al. 2015; McClintock et al. 2018). The behaviour we see in the CODEX sample would be expected if there were an increasing fraction of RS galaxies over cosmic time, with no evolution in the overall halo occupation number N_{200} of galaxies within the virial region above a particular stellar mass or luminosity cut. The redshift trend we measure is in rough agreement with results from Hennig et al. (2017), a study of the galaxy populations in 74 SPT clusters whose redshifts extend to $z \sim 1.1$ and that were imaged as part of the DES-SV survey. They find that the number of RS galaxies $N_{200,RS}$ brighter than $m_* + 2$ and within r_{200c} decreases with redshift at fixed mass as $N_{200,RS} \propto (1+z)^{-0.84 \pm 0.34}$, corresponding to an evolution of the RS fraction within r_{200c} going as $f_{RS} \propto (1+z)^{-0.65 \pm 0.21}$. This evolution is less steep than the λ -mass evolution we observe here, but the two results are statistically consistent with a difference of 0.48 ± 0.63 .

In contrast, the McClintock et al. (2018) and Saro et al. (2015) results show no redshift trend with $\gamma_{\lambda} = -0.22 \pm 0.22$ and 0.60 ± 0.63 , respectively. These results differ from our measurement at 1.5σ (0.91 ± 0.63) and 2σ (1.73 ± 0.86), respectively. Interestingly, as discussed in Section 4.2.1, our measured redshift trend is closer to that measured in the other two analyses when we include more high-redshift clusters that are sampled by smaller numbers of spectroscopic redshifts. Clearly, further study is needed to better understand whether there is a difference in the redshift trend inferred from dynamical masses and to pinpoint any underlying causes.

5 CONCLUSIONS

In this paper, we present a richness–mass–redshift scaling relation calibration using galaxy dynamical information from a sample of 428 CODEX galaxy clusters. These are X-ray-selected systems from RASS that have RS-selected redMaPPer optical counterparts within a search radius of 3 arcmin. Our sample has redshifts up to $z \sim 0.66$ and optical richnesses $\lambda \geq 20$. The spectroscopic follow-up comes from the SPIDERS survey, resulting in 7807 red member galaxies after interloper rejection and the exclusion of all systems with fewer than 10 member redshifts.

We study the λ - M_{200c} - z relation by extracting the likelihood of consistency between the velocity sample for each individual cluster and the modelled projected phase space velocity distribution for a cluster of inferred mass M_{200c} given its observed λ and redshift z . The modelling is carried out using a Jeans analysis based on the code MAMPOSSt (Mamon et al. 2013), which allows us to build the projected phase space velocity distributions for clusters of particular mass, given a range of models for the orbital anisotropy of the

galaxies. In our analysis, we adopt an NFW mass profile and employ five different velocity dispersion anisotropy profiles. Furthermore, we adopt an NFW profile for the red galaxy tracer population with concentration $c = 5.37$ (Hennig et al. 2017, and Section 2.5). We combine results from the different anisotropy models by performing Bayesian model averaging, allowing us to effectively marginalize over the orbital anisotropy of the spectroscopic galaxy population.

We model the scaling relation as $\lambda \propto A_\lambda M_{200c}^{B_\lambda} (1+z)^{\gamma_\lambda}$ (equation 5). As described in Section 4.1, we apply corrections for the Eddington bias and for the Malmquist bias. Results are presented in Table 2. For clusters at our pivot redshift of $z_{\text{piv}} = 0.18$ and pivot mass of $M_{\text{piv}} = 3 \times 10^{14} M_\odot$, we find our constraints on the scaling relation to be as follows: the normalization A_λ , mass slope B_λ and redshift slope γ_λ are

$$\begin{aligned} A_\lambda &= 38.6_{-4.1}^{+3.1} \pm 3.9, \\ B_\lambda &= 0.99_{-0.07}^{+0.06} \pm 0.04, \\ \gamma_\lambda &= -1.13_{-0.34}^{+0.32} \pm 0.49. \end{aligned} \quad (12)$$

As discussed in Section 4.2, the quoted uncertainties include a 10 percent systematic uncertainty on the dynamical mass that is applied wholly to the scaling relation amplitude (see study of systematics in Mamon et al. 2013) and a systematic uncertainty of 0.49 on the redshift trend γ_λ , that arises from sensitivity in our redshift trend parameter to cuts on the cluster sample according to the number of member galaxies with spectroscopic redshifts.

Our results on the mass trend of the λ –mass scaling relation are in generally good agreement with previous studies of the mass dependence of the halo occupation number, or the number of cluster galaxies within a common portion of the luminosity function (often $m_* + 2$) and within a common portion of the cluster virial region (typically defined using r_{500} or r_{200}) (Lin et al. 2004; Hennig et al. 2017). This is an indication that the redMaPPer algorithm is effective at selecting cluster galaxies over a common portion of the virial region and that the galaxy RS fraction is not a strong function of cluster mass in this mass range.

Moreover, our results are in good agreement with those from previous studies of the λ –mass relation using SPT-selected clusters that have been cross-matched with DES SV identified optical systems (Saro et al. 2015). We are also consistent with the value of the mass trend measured using cluster clustering in SDSS (Baxter et al. 2016) and CMB lensing of the DES Y1 redMaPPer sample using SPT (Baxter et al. 2018). On the other hand, our results are in disagreement with a study of redMaPPer clusters detected in SDSS data (Simet et al. 2017) and show a $\sim 2.7\sigma$ tension with the constraints obtained from redMaPPer galaxy clusters identified in the DES Y1 data (McClintock et al. 2018). Both of these latter results arose from the analysis of stacked weak lensing signatures, and neither analysis sought to obtain the true underlying λ –mass relation after correction for the Eddington bias. As discussed in Section 4.3.1, the Eddington bias correction would not be large enough to explain the difference. We suggest instead that the difference is reflective of the likely differences in the contamination of a pure redMaPPer sample and our CODEX sample, which is first X-ray selected and then cross-matched to the redMaPPer candidates within 3 arcmin radius.

In Section 4.3.1, we also discuss two scaling relation calibrations that adopt redMaPPer counts together with either stacked weak lensing or cluster clustering to calibration the richness–mass relation. Inferring cluster mass information from the counts such as in those two analyses requires an accurate description of the contamination

or projection effects in the redMaPPer sample. Interestingly, our dynamical mass calibration results are in good agreement with the counts + clustering analysis (Jimeno et al. 2017), but not with the counts + stacked weak lensing analysis (Murata et al. 2018), where the authors find a dramatically larger scatter in richness–mass is required to bring their weak lensing and counts constraints on cluster masses into agreement.

The redshift trend γ_λ of our richness–mass relation shows a strong negative trend where λ at fixed mass decreases with redshift. This result can be interpreted as an indication of the increasing fraction of cluster RS galaxies over cosmic time. As presented in Section 4.3.2, our results are somewhat steeper than but statistically consistent with those from Hennig et al. (2017), where they studied SPT-selected clusters and found that the fraction of RS galaxies to $m_*(z) + 2$ decreases with redshift, from ~ 80 per cent at $z \sim 0.1$ to ~ 55 per cent at $z \sim 1$, following the form $f_{\text{RS}} \propto (1+z)^{-0.65 \pm 0.21}$. Our measurement is steeper than other results showing little or no redshift trend in the λ –mass relation (Saro et al. 2015; McClintock et al. 2018), but the differences are only significant at 1.5σ and 2σ , respectively. Further study of the redshift trend of the λ –mass relation is clearly warranted.

In addition, we test the impact of interesting selection effects on our results in Section 4.2.2. We show that negative covariance between the scatter in X-ray luminosity and the scatter in optical richness for clusters at the levels measured in the CODEX sample has negligible impact on the λ –mass relation.

In summary, dynamical masses are a powerful tool to gain information on the link between the masses of galaxy clusters and readily obtainable observables – even in the limit of large cluster samples with small spectroscopic samples available for each cluster. Further work to perform a dynamical analysis on numerical simulations of structure formation will be crucial to being able to properly assess the true precision and robustness of the dynamical masses and anisotropy measurements we seek to extract from the data. A better understanding of the expected variation of the velocity anisotropy profile, of the distribution of interlopers after cleaning and of the impact of departures from equilibrium on our Jeans analysis will be broadly helpful. Our analysis demonstrates that there is promise in the analysis of small per-cluster spectroscopic samples of the sort that will be delivered by future spectroscopic surveys like DESI (Levi et al. 2013), 4MOST (de Jong et al. 2012), and Euclid (Laureijs et al. 2011).

ACKNOWLEDGEMENTS

RC would like to thank Gus Evrard, Arya Farahi, Tom McClintock, and Steffen Hagstotz for helpful discussions. The Munich group acknowledges the support by the DFG Cluster of Excellence ‘Origin and Structure of the Universe’, the Transregio program TR33 ‘The Dark Universe’, the MPG faculty fellowship program and the Ludwig-Maximilians-Universität Munich. RC acknowledges participation in the IMPRS on Astrophysics at the Ludwig-Maximilians University and the associated financial support from the Max-Planck Society. RC and VS acknowledge support from the German Space Agency (DLR) through *Verbundforschung* project ID 50OR1603. AS is supported by the ERC-StG ‘ClustersXCosmo’, grant agreement 716762. AB acknowledges the hospitality of the LMU and partial financial support from PRIN-INAF 2014 ‘Glittering kaleidoscopes in the sky: the multifaceted nature and role of Galaxy Clusters?’, PI: Mario Nonino.

Funding for the SDSS-IV has been provided by the Alfred P. Sloan Foundation, the U.S. Department of Energy Office of Science,

and the Participating Institutions. SDSS-IV acknowledges support and resources from the Center for High-Performance Computing at the University of Utah. The SDSS web site is www.sdss.org.

SDSS-IV is managed by the Astrophysical Research Consortium for the Participating Institutions of the SDSS Collaboration including the Brazilian Participation Group, the Carnegie Institution for Science, Carnegie Mellon University, the Chilean Participation Group, the French Participation Group, Harvard-Smithsonian Center for Astrophysics, Instituto de Astrofísica de Canarias, The Johns Hopkins University, Kavli Institute for the Physics and Mathematics of the Universe (IPMU) / University of Tokyo, the Korean Participation Group, Lawrence Berkeley National Laboratory, Leibniz Institut für Astrophysik Potsdam (AIP), Max-Planck-Institut für Astronomie (MPIA Heidelberg), Max-Planck-Institut für Astrophysik (MPA Garching), Max-Planck-Institut für Extraterrestrische Physik (MPE), National Astronomical Observatories of China, New Mexico State University, New York University, University of Notre Dame, Observatório Nacional/MCTI, The Ohio State University, Pennsylvania State University, Shanghai Astronomical Observatory, United Kingdom Participation Group, Universidad Nacional Autónoma de México, University of Arizona, University of Colorado Boulder, University of Oxford, University of Portsmouth, University of Utah, University of Virginia, University of Washington, University of Wisconsin, Vanderbilt University, and Yale University.

REFERENCES

- Aihara H. et al., 2011, *ApJS*, 193, 29
 Annis J. et al., 2014, *ApJ*, 794, 120
 Baxter E. J. et al., 2018, *MNRAS*, 476, 2674
 Baxter E. J., Rozo E., Jain B., Rykoff E., Wechsler R. H., 2016, *MNRAS*, 463, 205
 Becker M. R., Kravtsov A. V., 2011, *ApJ*, 740, 25
 Beers T. C., Flynn K., Gebhardt K., 1990, *AJ*, 100, 32
 Binney J., Tremaine S., 1987, *Galactic Dynamics*. Princeton Univ. Press, Princeton, NJ, p. 747
 Biviano A. et al., 2013, *A&A*, 558, A1
 Biviano A., Girardi M., 2003, *ApJ*, 585, 205
 Biviano A., Popesso P., Dietrich J. P., Zhang Y.-Y., Erfanianfar G., Romaniello M., Sartoris B., 2017, *A&A*, 602, A20
 Blanton M. R. et al., 2017, *AJ*, 154, 28
 Bulbul E. et al., 2018, *ApJ*, 871, 50
 Capasso R. et al., 2019, *MNRAS*, 482, 1043
 Carlberg R. G. et al., 1997, *ApJ*, 485, L13
 Clerc N. et al., 2016, *MNRAS*, 463, 4490
 Clerc N. et al., 2018, *A&A*, 617, A92
 Corless V. L., King L. J., 2009, *MNRAS*, 396, 315
 Costanzi M. et al., 2018, *MNRAS*, 482, 490
 Dawson K. S. et al., 2016, *AJ*, 151, 44
 de Haan T. et al., 2016, *ApJ*, 832, 95
 de Jong R. S. et al., 2012, in *Proc. SPIE Conf. Ser. Vol. 8446, Ground-based and Airborne Instrumentation for Astronomy IV*. SPIE, Bellingham, p. 84460T
 de Propris R., Stanford S. A., Eisenhardt P. R., Dickinson M., Elston R., 1999, *AJ*, 118, 719
 Diemer B., 2017, *ApJS*, 239, 35
 Dietrich J. P. et al., 2018, *MNRAS*, 483, 2871
 Dressler A., 1984, *ARA&A*, 22, 185
 Dutton A. A., Macciò A. V., 2014, *MNRAS*, 441, 3359
 Evrard A. E. et al., 2008, *ApJ*, 672, 122
 Farahi A., Evrard A. E., Rozo E., Rykoff E. S., Wechsler R. H., 2016, *MNRAS*, 460, 3900
 Feroz F., Hobson M. P., 2008, *MNRAS*, 384, 449
 Feroz F., Hobson M. P., Bridges M., 2009, *MNRAS*, 398, 1601
 Feroz F., Hobson M. P., Cameron E., Pettitt A. N., 2013, preprint ([arXiv:1306.2144](https://arxiv.org/abs/1306.2144))
 Gladders M. D., Yee H. K. C., Majumdar S., Barrientos L. F., Hoekstra H., Hall P. B., Infante L., 2007, *ApJ*, 655, 128
 Gunn J. E. et al., 2006, *AJ*, 131, 2332
 Haiman Z., Mohr J. J., Holder G. P., 2001, *ApJ*, 553, 545
 Haines C. P. et al., 2018, *MNRAS*, 477, 4931
 Hennig C. et al., 2017, *MNRAS*, 467, 4015
 Hoeting J. A., Madigan D., Raftery A. E., Volinsky C. T., 1999, *Stat. Sci.*, 14, 382
 Jimeno P., Broadhurst T., Lazkoz R., Angulo R., Diego J.-M., Umetsu K., Chu M.-c., 2017, *MNRAS*, 466, 2658
 Katgert P., Biviano A., Mazure A., 2004, *ApJ*, 600, 657
 Klein M. et al., 2018, *MNRAS*, 474, 3324
 Klein M., Grandis S., Mohr J., Paulus M., the DES Collaboration, 2019, preprint ([arXiv:1812.09956](https://arxiv.org/abs/1812.09956))
 Laureijs R. et al., 2011, preprint ([arXiv:1110.3193](https://arxiv.org/abs/1110.3193))
 Levi M. et al., 2013, preprint ([arXiv:1308.0847](https://arxiv.org/abs/1308.0847))
 Lin Y.-T., Mohr J. J., Stanford S. A., 2004, *ApJ*, 610, 745
 Lin Y.-T., Mohr J. J., Gonzalez A. H., Stanford S. A., 2006, *ApJ*, 650, L99
 Macciò A. V., Dutton A. A., van den Bosch F. C., 2008, *MNRAS*, 391, 1940
 Mamon G. A., Łokas E. L., 2005, *MNRAS*, 363, 705
 Mamon G. A., Biviano A., Murante G., 2010, *A&A*, 520, A30
 Mamon G. A., Biviano A., Boué G., 2013, *MNRAS*, 429, 3079
 Mantz A. B. et al., 2015, *MNRAS*, 446, 2205
 McClintock T. et al., 2018, *MNRAS*, 482, 1352
 Mei S. et al., 2009, *ApJ*, 690, 42
 Merloni A. et al., 2012, preprint ([arXiv:1209.3114](https://arxiv.org/abs/1209.3114))
 Merritt D., 1985, *MNRAS*, 214, 25P
 Merritt D., 1987, *ApJ*, 313, 121
 Merritt D., Graham A. W., Moore B., Diemand J., Terzić B., 2006, *AJ*, 132, 2685
 Mirkazemi M. et al., 2015, *ApJ*, 799, 60
 Mortonson M. J., Hu W., Huterer D., 2011, *Phys. Rev. D*, 83, 023015
 Munari E., Biviano A., Mamon G. A., 2014, *A&A*, 566, A68
 Murata R., Nishimichi T., Takada M., Miyatake H., Shirasaki M., More S., Takahashi R., Osato K., 2018, *ApJ*, 854, 120
 Muzzin A. et al., 2012, *ApJ*, 746, 188
 Navarro J. F. et al., 2010, *MNRAS*, 402, 21
 Navarro J. F., Frenk C. S., White S. D. M., 1996, *ApJ*, 462, 563
 Navarro J., Frenk C., White S., 1997, *ApJ*, 490, 493
 Okabe N., Zhang Y.-Y., Finoguenov A., Takada M., Smith G. P., Umetsu K., Futamase T., 2010, *ApJ*, 721, 875
 Osipkov L. P., 1979, *SvA Lett.*, 5, 42
 Pacaud F. et al., 2016, *A&A*, 592, A2
 Planck Collaboration XIII et al., 2016, *A&A*, 594, A13
 Powell, 2006, in *Large-Scale Nonlinear Optimization*. Springer, US
 Pratt G. W., Böhringer H., Croston J. H., Arnaud M., Borgani S., Finoguenov A., Temple R. F., 2007, *A&A*, 461, 71
 Predehl P. et al., 2010, in Arnaud M., Murray S. S., Takahashi T., eds, *Proc. SPIE, Vol. 7732, Space Telescopes and Instrumentation 2010: Ultraviolet to Gamma Ray*. SPIE, Bellingham, p. 77320U
 Rines K. J., Geller M. J., Diaferio A., Hwang H. S., Sohn J., 2018, *ApJ*, 862, 172
 Ruel J. et al., 2014, *ApJ*, 792, 45
 Rykoff E. S. et al., 2012, *ApJ*, 746, 178
 Rykoff E. S. et al., 2014, *ApJ*, 785, 104
 Rykoff E. S. et al., 2016, *ApJS*, 224, 1
 Sandage A., 2000, *Malmquist Bias and Completeness Limits*, CRC Press, Boca Raton, FL, p. 1940
 Saro A. et al., 2015, *MNRAS*, 454, 2305
 Saro A. et al., 2017, *MNRAS*, 468, 3347
 Saro A., Mohr J. J., Bazin G., Dolag K., 2013, *ApJ*, 772, 47
 Sereno M., Ettori S., 2017, *MNRAS*, 468, 3322
 Sifón C. et al., 2013, *ApJ*, 772, 25

- Simet M., McClintock T., Mandelbaum R., Rozo E., Rykoff E., Sheldon E., Wechsler R. H., 2017, *MNRAS*, 466, 3103
- Soergel B. et al., 2016, *MNRAS*, 461, 3172
- Sohn J., Geller M. J., Rines K. J., Hwang H. S., Utsumi Y., Diaferio A., 2018, *ApJ*, 856, 172
- Song J., Mohr J. J., Barkhouse W. A., Warren M. S., Dolag K., Rude C., 2012, *ApJ*, 747, 58
- Spergel D. N. et al., 2003, *ApJS*, 148, 175
- Strazzullo V. et al., 2018, *A&A*, 622, A117
- Tinker J., Kravtsov A. V., Klypin A., Abazajian K., Warren M., Yepes G., Gottlöber S., Holz D. E., 2008, *ApJ*, 688, 709
- Tiret O., Combes F., Angus G. W., Famaey B., Zhao H. S., 2007, *A&A*, 476, L1
- Umetsu K., Broadhurst T., Zitrin A., Medezinski E., Coe D., Postman M., 2011, *ApJ*, 738, 41
- van der Burg R. F. J., Hoekstra H., Muzzin A., Sifón C., Balogh M. L., McGee S. L., 2015, *A&A*, 577, A19
- van der Marel R. P., Magorrian J., Carlberg R. G., Yee H. K. C., Ellingson E., 2000, *AJ*, 119, 2038
- Vikhlinin A., McNamara B. R., Forman W., Jones C., Quintana H., Hornstrup A., 1998, *ApJ*, 502, 558
- Voges W. et al., 1999, *A&A*, 349, 389
- White S. D. M., Efstathiou G., Frenk C. S., 1993, *MNRAS*, 262, 1023

This paper has been typeset from a $\text{\TeX}/\text{\LaTeX}$ file prepared by the author.